This is a repository copy of *Laboratory measurements of heterogeneous CO2 ice nucleation on nanoparticles under conditions relevant to the Martian mesosphere*.

Article:

Nachbar, M, Duft, D, Mangan, TP et al. (3 more authors) (2016) Laboratory measurements of heterogeneous CO2 ice nucleation on nanoparticles under conditions relevant to the Martian mesosphere. Journal of Geophysical Research: Planets, 121 (5). pp. 753-769. ISSN 2169-9097

https://doi.org/10.1002/2015JE004978

Laboratory measurements of heterogeneous CO_2 ice nucleation on nanoparticles under conditions relevant to the Martian mesosphere

Mario Nachbar[1], Denis Duft[2], Thomas Peter Mangan[3], Juan Carlos Gomez Martin[3], John M. C. Plane[3] and Thomas Leisner[1,2]

[1]Institute of Environmental Physics, University of Heidelberg, Heidelberg, Germany
[2]Institute for Meteorology and Climate Research, Karlsruhe Institute of Technology – KIT, Karlsruhe, Germany
[3]School of Chemistry, University of Leeds, Leeds, United Kingdom

Corresponding author: Mario Nachbar (mario.nachbar@kit.edu)

Key Points:

- Measurements on heterogeneous nucleation of CO_2 on meteoric smoke particle analogues
- Evaluation of contact parameter, desorption energy and sticking coefficient
- Extreme cold conditions are needed to affect CO_2 nucleation in the Martian mesosphere

Abstract

Clouds of CO_2 ice particles have been observed in the Martian mesosphere. These clouds are believed to be formed through heterogeneous nucleation of CO_2 on nanometer-sized meteoric smoke particles (MSPs) or upward propagated Martian dust particles (MDPs). Large uncertainties still exist in parameterizing the microphysical formation process of these clouds as key physico-chemical parameters are not well known. We present measurements on the nucleation and growth of CO_2 ice on sub 4 nm radius iron oxide and silica particles representing MSPs at conditions close to the mesosphere of Mars. For both particle materials we determine the desorption energy of CO_2 to be $\Delta F_{des} = (18.5 \pm 0.2)\ \mathrm{kJ\ mol^{-1}}$ corresponding to $\Delta F_{des} = (0.192 \pm 0.002)$ eV and obtain $m = 0.78 \pm\ 0.02$ for the contact parameter that governs heterogeneous nucleation by analyzing the measurements using classical heterogeneous nucleation theory. We did not find any temperature dependence for the contact parameter in the temperature range examined (64 K to 73 K). By applying these values for MSPs in the Martian mesosphere, we derive characteristic temperatures for the onset of CO_2 ice nucleation, which are 8 - 18 K below the CO_2 frost point temperature, depending on particle size. This is in line with the occurrence of highly supersaturated conditions extending to 20 K below frost point temperature without the observation of clouds. Moreover, the sticking coefficient of CO_2 on solid CO_2 was determined to be near unity. We

This article has been accepted for publication and undergone full peer review but has not been through the copyediting, typesetting, pagination and proofreading process which may lead to differences between this version and the Version of Record. Please cite this article as doi: 10.1002/2015JE004978

further argue that the same parameters can be applied to CO_2 nucleation on upward propagated MDPs.

1 Introduction

Reflections at 4.3 µm in the infrared spectra recorded by Mariner 6 and 7 were the first measurements which indicated that solid CO_2 ice could actually be present in the upper atmosphere of Mars [Herr and Pimentel, 1970]. A mesospheric cloud was then observed from the planet surface by the Mars rover Pathfinder in 1997 [Smith et al., 1997]. Since the temperature profile measured by Pathfinder during its entry process revealed temperatures well below the frost point temperature of CO_2 at a height of about 80km $\left(T_{frost} \approx 102\,\mathrm{K}\right)$ [Magalhães et al., 1999], these clouds were argued to consist of CO_2 [Clancy and Sandor, 1998], the main constituent of the Martian atmosphere (95%). The first conclusive proof of the existence of CO_2 clouds in the Martian mesosphere was then provided by the imaging spectrometer OMEGA on board Mars Express [Montmessin et al., 2007].
After the Pathfinder discovery, CO_2 ice clouds have been observed many times in the Martian mesosphere [e.g. Clancy et al., 2007; Määttänen et al., 2010; Montmessin et al., 2007; Montmessin et al., 2006; Vincendon et al., 2011]. These clouds mainly appear during pre- and post-aphelion season, which are the coldest periods in the mesosphere of Mars. Thermal tides and gravity waves are strongest at tropical latitudes [Creasey et al., 2006] and are believed to cause cold pockets with temperatures well below the CO_2 frost point temperature in the mesosphere, thereby inducing the heterogeneous formation of CO_2 clouds [Gonzalez-Galindo et al., 2011; Spiga et al., 2012]. Two main types of mesospheric clouds have been reported, one during day at equatorial latitudes at heights between 60 km and 85 km with mean particle radii exceeding 1 µm [Montmessin et al., 2007], and the other during night at subtropical latitudes at heights between 80 km and 100 km with particle radii of about 100 nm [Montmessin et al., 2006]. In addition, Määttänen et al. [2010] identified three mesospheric midlatitude autumn clouds. The variation in cloud pattern between day and night was reproduced in a recent model study by Listowski et al. [2014], in which nucleation was activated by gravity wave-perturbed temperature profiles.

Vincendon et al. [2011] found that CO_2 clouds are the dominant type of clouds in the mesosphere of Mars, but also water ice clouds can occur up to a height of 80 km. This result is in agreement with a water vapor measurement performed by Maltagliati et al. [2013] showing water vapor concentrations above ice saturation up to this height during southern spring. However, during that time of the year almost no CO_2 ice clouds have been observed. Within the main occurrence period of CO_2 ice clouds no H_2O supersaturated conditions could be detected above a height of 50 km [Maltagliati et al., 2011; Maltagliati et al., 2013].

Although great progress has been made in the last decade in monitoring and modeling mesospheric CO_2 clouds on Mars, large uncertainties remain regarding the microphysical formation processes of the ice particles: Homogeneous nucleation of CO_2 in the mesosphere would require extremely cold conditions (about 50 K below frost point temperature) [Määttänen et al., 2010], and these have never been observed. Also, ion-induced nucleation requires CO_2 saturation levels too high to compete with heterogeneous nucleation [Listowski et al., 2014]. Consequently, the most likely formation process of mesospheric CO_2 clouds on Mars is heterogeneous nucleation, with the nature of the CO_2-ice nuclei still under discussion. In addition to upward propagating Martian dust particles (MDPs), meteoric smoke particles (MSPs) produced from the ablation and recondensation of meteoric material could potentially serve as ice nuclei. The peak meteoric ablation height on Mars is estimated to occur at a height between 50 km and 90 km [Adolfsson et al., 1996; Whalley and Plane, 2010], being consistent with the altitude where CO_2 clouds have been observed. The major elemental constituents of meteoroids (besides O) are Fe, Mg and Si, which should ablate with similar efficiencies [Vondrak et al., 2008]. The resulting atoms are then oxidized by O_2, O_3, H_2O and CO_2 to form oxides, hydroxides and carbonates which are presumably the building blocks of MSPs [Plane et al., 2015]. The produced MSPs with radii between 1 nm – 10 nm (if assumed to be as large as on Earth) [Bardeen et al., 2008] are believed to be about one order of magnitude smaller than MDPs [Listowski et al., 2014]. The ability of a particle to nucleate CO_2 is described in classical heterogeneous nucleation theory by the desorption energy ΔF_{des} and the contact parameter m. If these parameters are known for MDPs as well as MSPs, measured temperature and CO_2 concentration profiles during the observation of CO_2 clouds in the mesosphere of Mars could be used in models like the 1D microphysical model of Listowski et al [2014] to evaluate the respective particle sizes and concentrations required to form the observed clouds. In this way, it might be possible to unravel the major type of nuclei forming Martian mesospheric CO_2 clouds. Here, the most critical unknown is the nucleation ability of the particles, due to a lack of CO_2 nucleation measurements on realistic particle materials, CO_2 concentrations (10^{15} to $10^{21}\mathrm{m}^{-3}$) and temperatures (70 to 115 K).

Currently a contact parameter of 0.952 determined experimentally by Glandorf et al. [2002] is predominantly used to describe nucleation in the mesosphere of Mars [Colaprete et al., 2008; Listowski et al., 2014]. This value for the contact parameter was measured on a water ice covered planar surface at temperatures between 130 and 140 K, which are about 20 to 50 K above the temperatures at which CO_2 clouds were observed in the Martian mesosphere. If this contact parameter is applied to Martian mesospheric CO_2 concentrations and particle radii between 2 and 100 nm, CO_2 nucleation would become efficient at temperatures between 2 and 11 K below saturation (i.e. frost-point) temperature. In contrast, Forget et al. [2009] and Montmessin et al. [2011] observed night time temperatures down to 20 K below frost point in the absence of clouds. These observations can either be explained by a lack of nuclei, or by a lower CO_2 nucleation ability of the present nuclei. The latter could be a result of a decrease of the contact parameter with temperature or because the nuclei are not water ice-covered and exhibit a lower contact parameter.

The discussion above highlights the need of laboratory experiments examining nucleation and growth of CO_2 on MSP and MDP analogues at Martian mesospheric conditions. Furthermore, such experiments may help to understand the influence of CO_2 clouds on past and current Martian climate, since CO_2 ice clouds might have played an important role in heating up the Martian atmosphere about 4 billion years ago so that liquid water was present at the surface [Forget and Pierrehumbert, 1997; Forget et al., 2013; Mischna et al., 2000; Wordsworth et al., 2013].

In this contribution, we present laboratory results on the nucleation and growth of CO_2 ice on singly charged nanometer-sized silica and iron oxide particles. These studies utilize a novel experimental setup which allows us to observe and analyze MSP analogues at conditions reasonably close to the Martian mesosphere. In section 2, we briefly review this setup. Section 3 gives the experimental results in terms of desorption energy, contact parameter and sticking coefficient. Finally, in section 4 we discuss the results and their implications to our understanding of cloud formation in the Martian mesosphere. Appendix A explains in some detail the growth rate and nucleation theory used to analyze the experimental data.

2 Experimental Method

We use a non-thermal low pressure (60 mbar) microwave plasma particle source (max. power 1250W at 2.45 GHz) to produce MSP analogues in the sub-4 nm radius regime. The synthesis of microwave-generated metal oxide particles and their characterization by particle mass spectrometry (PMS) and transmission electron microscopy (TEM) are well described in the literature [e.g Baumann et al., 2006; Giesen et al., 2005; Janzen et al., 2002]. A flow of 3 standard liters per minute (slm) of helium carrying trace amounts of organometallic precursors and oxygen is passed through the microwave plasma source to produce sub-4 nm radius MSP analogues. The precursors Ferrocene ($\mathrm{Fe(C_5H_5)_2}$), Tetraethyl orthosilicate ($\mathrm{C_8H_{20}O_4Si}$) and Magnesocene ($\mathrm{Mg(C_5H_5)_2}$) are separately evaporated and mixed into the helium flow. The concentration of precursor molecules in the microwave plasma is controlled by adjusting the precursor reservoir temperatures. We assume that the precursor molecules completely decompose in the plasma. Addition of 0.3 slm of an oxygen/helium mixture (20 % of oxygen) upstream of the plasma results in oxidation of the Fe, Si and Mg atoms released from the break-up of the organometallic precursors at the microwave discharge and the subsequent generation of particles based on these oxides. In addition, carbon-bearing break-up products are oxidized to CO_2, which precludes their insertion in particles. Microwave-generated particles produced in similar experimental arrangements have been shown to be single charged, compact and spherical with a very small degree of agglomeration [e.g Baumann et al., 2006; Giesen et al., 2005; Janzen et al., 2002]. Since the composition of mixed Mg-Fe-silicate particles produced with this method has not been sufficiently characterized, in this work we present only experiments using SiO_2 ($\rho = 2.3\,\mathrm{kgm^{-3}}$) and Fe_xO_y ($\rho = 5.2\,\mathrm{kgm^{-3}}$) particles. In the future we will also perform experiments on magnesium oxide and mixed Mg-Fe-silicate particles which will be accompanied with an analysis of their stoichiometric composition.

A detailed description of the Trapped Reactive Atmospheric Mass Spectrometer (TRAPS) and the Molecular flow Ice Cell (MICE) employed in this study can be found elsewhere [Duft et al., 2015; Meinen et al., 2010]. Briefly, the produced MSP analogues are transferred and focused via the gas flow into a vacuum chamber using an aerodynamic lens accompanied with differential pumping. Within the chamber the single positively-charged particles are mass selected using a quadrupole deflector, and subsequently stored in MICE. This device consists of a linear ion trap which applies mesospheric conditions of pressure, temperature and supersaturation to the electro-dynamically trapped particle cloud. As discussed in [Duft et al., 2015], MICE has CO_2 ice covered surfaces acting as a source for CO_2 molecules according to the vapor pressure at the adjusted wall temperature in the range between 60 and 90 K. The CO_2 concentration at the particle location is calculated from the geometry of MICE and the vapor pressure of CO_2 at the wall temperature. For the vapor pressure over a solid CO_2 surface we use the parameterization given by [James et al., 1992]. The wall temperatures in MICE are always kept above the CO_2 glass transition temperature at 50 K [Souda, 2006] to avoid ambiguity in CO_2 ice structure and hence to CO_2 vapor pressure, density and surface tension. During storage in MICE the trapped particles are thermalized by collisions with an additional superabundant Helium background gas of about 0.3 Pa. The Helium gas temperature is determined by the temperature of the CO_2 ice covered surfaces surrounding the particles. Slight temperature gradients across MICE and a measurement uncertainty of about 0.1 K result in a particle temperature uncertainty of about 0.4 K and an uncertainty of the CO_2 concentration of about 10 %.

In a typical experimental run about 10^7 mass selected singly-charged particles are filled into MICE within one second and are stored for a selectable amount of time at constant particle temperature and CO_2 concentration. Depending on the applied conditions, adsorption, nucleation and subsequent depositional growth of the supersaturated atmospheric component (in this case CO_2) occurs. These processes can be observed by extracting small samples of the particle population during each run after periodic trap residence times to a time-of-flight mass spectrometer (TOF-MS) for analysis of the trapped particle mass distribution. As there are only slight inhomogeneities of particle temperature and CO_2 concentration across MICE [Duft et al., 2015], which are considered in the given measurement uncertainties, the extracted samples can be regarded as representative for the whole particle population trapped in MICE. The distribution of recorded particle time-of-flights is converted to a particle mass distribution, which can be fitted reasonably well using a Gauss curve. The approximately Gaussian shape of the distribution and deviations from it result from the specific design of the ion acceleration zone in the TOF-MS. For the analysis of the particle mass data we used the maximum of the recorded mass distribution as the most frequent particle mass (modal value) with the standard deviation (5 to 7 %) of the Gaussian fit as a 1σ uncertainty interval. The measured TOF spectra result from the convolution of the instrumental sampling function and the mass distribution of particles trapped in MICE. The actual width of the particle mass distribution trapped in MICE is thus smaller than the width of the measured TOF spectra. Using the standard deviation of the measured TOF spectra as an uncertainty guarantees that we do not underestimate the width of the particle mass distribution.

As described earlier [Duft et al., 2015], the device is subject to some limitations depending on the type of vapor that is to be deposited onto the trapped particles. For the case of CO_2 MICE is able to produce supersaturated conditions at temperatures between 60 and 90 K. Due to the high supersaturation required for the onset of nucleation, the range of particle temperatures nucleation and growth was actually examined in MICE was limited to temperatures between 62 and 73 K. These temperatures are somewhat colder but reasonably close to the temperature range of interest in the Martian mesosphere (75 K – 100 K).

3 Results

Singly charged iron oxide and silica particles of variable but well known initial mass were exposed to a controlled supersaturation of CO_2 at temperatures between 62 and 73 K. Time-dependent particle mass distributions were recorded in the TOF-MS as a function of residence time under supersaturated conditions. The resulting mass growth curves have been analyzed using classical heterogeneous nucleation and growth theory, which is not reviewed here, but detailed in Appendix A. Tables 1, 2 and 3 list the experiments carried out respectively for the determination of the desorption energy, the sticking coefficient and the contact parameter. Each run consists of filling MICE and recording the time resolved mass of the trapped particles by extracting small samples of the trapped particle mass population after periodic residence times to the TOF spectrometer. All runs performed at the same day belong to one experiment number. Figure 1 shows a series of measurements of CO_2 nucleation and depositional growth on silica particles of 2.5 nm initial radius at three different particle temperatures. For this series of measurements the CO_2 concentration was set to a constant value, in this case $n_{CO_2} = 5 \cdot 10^{15}\ \mathrm{m}^{-3}$, while the particle temperature and therefore saturation was varied. Saturation values have been calculated according to:

$$S = \frac{p_{CO_2}}{p_{sat}(T_{part})} = \frac{n_{CO_2} \cdot k \cdot T_{part}}{p_{sat}(T_{part})} \qquad (1)$$

using the mean CO_2 concentration and the mean particle temperature. Due to the strong dependence of vapor pressure on temperature, the relative uncertainty in S amounts to about 25 to 30 %. At each experimental condition several runs were carried out and averaged. Three different growth modes can be distinguished in Figure 1. Curve a (Exp. 136, run 123-125 in

Table **1**) corresponds to a situation where the supersaturation is too low to activate nucleation and only adsorption of CO_2 molecules on the particle surface is observed. The amount of adsorbed CO_2 molecules increases with time until an equilibrium of adsorbing and desorbing molecules on the surface of the nucleus described by Eq. (A3) is reached. Note that for a particle temperature of about 68 K and saturation as high as 900, no nucleation occurs. At slightly lower temperature (curve b, Exp. 136, run 104-105 in Table 3) the supersaturation is high enough to activate nucleation followed by the depositional growth of CO_2. At the lowest temperature shown (curve c, Exp. 136, run 80-83 in Table 2), the nucleation rate is very high and the particles follow the growth regime from the beginning.

3.1 Desorption Energy

To describe the microphysical nucleation process in the Martian mesosphere we use classical heterogeneous nucleation induced by surface diffusion, which is summarized in Appendix A.1. This approach assumes that the adsorbed CO_2 molecules diffuse on the surface of the particle and can collide and combine to clusters of different sizes, which may eventually reach the critical size resulting in a nucleation event. Consequently, the concentration of monomers $c_{1,s}$ on the surface of the nucleus is a critical parameter governing nucleation. This concentration is calculated from the incoming and outgoing flux of CO_2 molecules, where the outgoing flux depends on the desorption energy ΔF_{des}, which is a characteristic property of the nucleus material. Measurements of particle mass as a function of residence time t_{res} under nucleation-free conditions (curve a in Figure 1) exhibit adsorption behavior only. Such measurements allow us to determine the desorption energy ΔF_{des} of CO_2 molecules on the particle material. In this case, the dependence of particle mass on residence time is described reasonably well by an empirical expression of the form

$$m(t) = m_0 + m_{ads} \cdot \left(1 - exp\left(\frac{-t_{res}}{\tau}\right)\right) \tag{2}$$

Equation (**2**) allows determining the total mass of adsorbed CO_2 molecules in equilibrium m_{ads} and therefore the amount of adsorbed CO_2 molecules on the surface of the particles with initial mass m_0. The fit of curve a) to Equation (2) is shown in Figure 1 by the green dotted line, which yields $m_{ads} = 53.8 \cdot 10^3$ atomic units corresponding to about 1200 CO_2 molecules. Corrected R^2 values of the exponential fits are typically larger than 0.99. Assuming sub-monolayer coverage, the surface concentration of adsorbed CO_2 monomers $c_{1,s}$ can be calculated. This has been done for silica particles with radii between 2.4 nm and 3.2 nm, and iron oxide particles with radii between 1.8 nm and 2.2 nm, at particle temperatures between 66 K and 73 K. Every $c_{1,s}$ value is divided by the CO_2 concentration in the gas phase yielding a quantity which, according to Equation (A3), only depends on temperature and ΔF_{des}. Experiment number, run number, particle size, particle temperature, CO_2 concentration, adsorbed mass of CO_2 molecules m_{ads} and the normalized $c_{1,s\,norm}$ values used for the desorption energy analysis are given in

Table **1**. The normalized $c_{1,s}$ values as a function of particle temperature for silica and iron oxide particles are shown in Figure . For each material, the average $c_{1,s\,norm}$ values have been fitted separately to Eq. (A3) using the Levenberg-Marquardt algorithm (LMA). The fitted curves are the red (iron oxide particles) and black (silica particles) lines in Figure . Corrected R^2 values of the fits are 0.92 for silica particles and 0.82 for iron oxide particles. In order to determine the uncertainty of the desorption energies, the same fitting exercise is carried out for the upper and lower limits of the normalized $c_{1,s}$ values, resulting in $\Delta F_{des} = (18.43 \pm 0.15)\ \mathrm{kJ\ mol^{-1}}$ for iron oxide particles and $\Delta F_{des} = (18.52 \pm 0.15)\ \mathrm{kJ\ mol^{-1}}$ for silica particles. The two values are in very good agreement within uncertainty, which leads to conclude that there is no significant difference between the desorption energy of both materials. Therefore, we recommend a common value of $\Delta F_{des} = (18.5 \pm 0.2)\ \mathrm{kJ\ mol^{-1}}$ for both materials, corresponding to $(0.192 \pm 0.002)\ \mathrm{eV}$. In order to account for the possibility of porous or fractal-shaped particles and agglomerates, the same analysis has been conducted assuming the particle surface area to be twice as large as for spherical particles, which yields a desorption energy that is only 2 % smaller.

3.2 Sticking Coefficient

The sticking coefficient is defined as the probability that a molecule is adsorbed when hitting a surface and is the equivalent of Maxwell's mass accommodation coefficient. This is equivalent to defining it as the ratio of total subliming flux with no impinging molecules present to the flux of impinging molecules at equilibrium vapor pressure. Thus, the sticking coefficient governs the rate of depositional mass accretion under conditions where mass accretion is not otherwise limited, e.g. by diffusional transport of the adsorbing molecules. The sticking coefficient is not required for nucleation theory but the precise measurement of particle mass as function of time under growth conditions allows us to determine the sticking coefficient for CO_2. In order to do this, the CO_2 deposition experiments at high supersaturation and thus high nucleation rate (e.g. curve c) in Figure 1 have been used. The deposition growth rate dm/dt has been evaluated at each point from the slope of the measured $m(t_{res})$ curve. The theoretical description of the deposition growth rate dm/dt is described in detail in Appendix A.2 where Eq. (A5) has been used to fit the determined growth rate data using α as the free parameter. We only consider data where the particles gained at least the mass corresponding to one monolayer of CO_2 molecules. Additionally, only measurements with S values above $3 \cdot 10^3$ have been analyzed, such that the flux of desorbing molecules is much smaller than the flux of adsorbing molecules. It has been assumed that particles are spherical and fully ice-covered. For not fully ice-covered particles we most likely underestimate the sticking coefficient. Measurements were performed on silica and iron oxide particles at CO_2 concentrations between $8 \cdot 10^{14}\ \mathrm{m^{-3}}$ and $2 \cdot 10^{16}\ \mathrm{m^{-3}}$ and particle temperatures between 61 K and 69 K. Experiment number, run number, initial particle size, particle temperature, CO_2 concentration and the determined sticking coefficient α are given in Table 2.

The values for the sticking coefficient are shown in Figure as a function of particle temperature. The major contribution to the error bars is a 10% uncertainty in the CO_2 concentration. The variation of the measured values is likely to result from additional measurement uncertainties as explained above. The paucity and scatter of the dataset do not allow any conclusions to be drawn about temperature dependence. In addition, it is reasonable to assume that the sticking coefficient of CO_2 on CO_2 ice-covered nuclei should be independent of the nucleus material. Therefore, the mean value of the combined dataset of iron oxide and silica particles has been computed. The mean value of $\alpha = 0.81 \pm 0.17$ is shown in Figure as a dashed blue line. Note that Weida et al. [1996] use an identical definition for the sticking coefficient and determined $\alpha = 1.0 \pm 0.2$ on a planar CO_2 surface at temperatures between 90 and 107 K.

3.3 Nucleation Rate and Contact Parameter

Nucleation rates on particles trapped in MICE at defined CO_2 concentration and particle temperature have been estimated and classical nucleation theory (Appendix A.1) has been used to determine the contact parameter m. The surface diffusion approach of classical nucleation theory assumes that the adsorbed CO_2 molecules diffuse on the surface of the particle and can collide and combine to clusters of different sizes, which may eventually reach the critical size resulting in a nucleation event. The concentration of monomers $c_{1,s}$ on the surface of the nucleus is a critical parameter governing nucleation rates with a ${c_{1,s}}^2$ dependency. In classical nucleation theory, $c_{1,s}$ is calculated by assuming a steady state equilibrium, where the flux of vapor molecules impinging and being adsorbed on the surface equals the flux of vapor molecules desorbing from the particle surface as given by Equation (A3). In contrast, in our experiments the trapped nanoparticles are not in steady state initially as they are not covered with CO_2, but acquire CO_2 molecules over time. The actual concentration of CO_2 monomers on the particle surface is thus a function of residence time in the particle trap in the presence of the CO_2 vapor phase. Therefore, the nucleation rate is a function of time in our experiments and increases during the adsorption process until either the critical surface concentration to induce nucleation or the equilibrium surface concentration is reached.

These arguments enable an insightful description of three different adsorption and mass growth regimes shown in Figure 1. Curve a) corresponds to adsorption growth only, i.e. after reaching the equilibrium state nucleation rates are too low to induce nucleation on a significant number of particles within the experimental time frame of 140 s. In this case, the mass growth is described by a simple exponential expression as discussed above (dotted green line inFigure 1). According to Equation (A3) the equilibrium surface concentration increases at lower particle temperature as shown by curve b). In this second regime, the mass growth curve initially follows a simple exponential growth (blue dotted line), and then diverges from the adsorption mode behavior at about 67 s residence time. Such deviation is interpreted as nucleation occurring on the trapped particles, enabling the transition to the mass growth regime under highly supersaturated conditions. Following the above argument that nucleation in adsorption mode is triggered by reaching a critical surface concentration, we can infer the critical surface concentration from the total mass of adsorbed CO_2 molecules at the transition point at 61 s (here $m_{ads} = 75.9 \cdot 10^3$ atomic units). It has to be noted that an increase in the width of the measured particle mass distributions of curve b) is not observed. This leads to the conclusion that nucleation-induced broadening of the particle mass distribution is insignificant, and nucleation on the majority of particles sets in within a time interval smaller than a few experimental time steps. Therefore, we estimate the nucleation rate at the critical surface concentration to be on the order of 1/(time step) which in this case is 1/(6 s). The nucleation rate and critical surface concentration can now be used with particle radius, temperature, ambient CO_2 concentration and their uncertainties to calculate the contact parameter m by numerically solving Equation (A1). This estimation of the nucleation rate is justified by the fact that by solving Equation (A1) the contact parameter is only a weak function of the nucleation rate, i.e. changing the nucleation rate by one order of magnitude results in a 1% change of m at the experimental conditions, which we add as an additional error in m in order to account for errors made in estimating the nucleation rate. Finally, at the lowest particle temperature and hence highest saturation corresponding to curve c) in Figure 1, transition to the growth regime cannot be observed anymore. At such high supersaturation nucleation already occurs during the adsorption process, i.e. in the first steep section of the curve. The rate of mass accretion in this first part of the growth is limited only by the supply of molecules from the vapor phase and is hence a function of particle surface area and CO_2 vapor pressure only.

Experiments to determine the nucleation rate and contact parameter were conducted with silica particles with initial radii between 2.4 nm and 3.1 nm, and iron oxide particles with initial radii between 1.9 nm and 2.1 nm. The CO_2 concentration was varied between $8 \cdot 10^{14}\ \mathrm{m}^{-3}$ and $4 \cdot 10^{17}\ \mathrm{m}^{-3}$ at particle temperatures between 64 K and 73 K. Experiment number, run number, initial particle size, particle temperature, CO_2 concentration, saturation, measured critical adsorbed mass of CO_2 molecules, determined nucleation rate and the calculated contact parameter m are given in Table 3. The contact parameters are shown in Figure as a function of particle temperature. Since the nucleation rate is very sensitive to particle temperature, the error of about 0.4 K in particle temperature is mainly responsible for the uncertainties in m. There is no significant trend of the contact parameter with the particle temperature and no difference can be determined between the particle materials. The mean value of m is determined to be $0.78 \pm\ 0.02$. In order to account for the possibility of porous or fractal-shaped particles and agglomerates, we performed the desorption energy analysis assuming the particle surface area to be twice as large as for spherical particles. This resulted in a 2% smaller desorption energy. Performing the contact parameter analysis assuming the particle surface area to be twice as large yields a mean contact parameter of 0.74 being only 5 % smaller.

4 Discussion

4.1 Sticking Coefficient, Desorption Energy and Contact Parameter

We have studied the nucleation and subsequent growth processes of CO_2 on nanometer-sized silica and iron oxide particles representing MSPs in the temperature range from 62 and 73 K. The sticking coefficient of CO_2 was determined to be 0.81 ± 0.17. The determined value compares well to a previous measurement of 1.0 ± 0.2 at temperatures between 90 and 107 K [Weida et al., 1996]. The two results combined indicate a near unity CO_2 sticking coefficient between 60 and 110 K. The desorption energy is essentially identical for iron oxide and silica particles and has been determined to be $\Delta F_{des} = (18.5 \pm 0.2)\ \mathrm{kJ\ mol^{-1}}$ corresponding to $\Delta F_{des} = (0.192 \pm 0.002)\ \mathrm{eV}$. Additionally, the mean value differs only by about 6 % from the value $\Delta F_{des} = 19.6\ \mathrm{kJ\ mol^{-1}}$determined for Mauna-Kea palagonite [Zent and Quinn, 1995] which is regarded as a terrestrial analogue for MDPs. Palagonite mainly consists of silica (≈45%), Fe_2O_3 (≈15%) and Al_2O_3 (≈20%) [Morris et al., 2000]. The contact parameter describes in step with the desorption energy how strongly a CO_2 molecule is bound to the nuclei surface. Thus, we assume that the tendency of the contact parameter between two materials behaves the same way as the desorption energy. Since iron, silicon and oxygen make up a large component of MDPs and the measured contact parameter of 0.78 ± 0.02 does not differ for iron oxide and silica particles as well, we conclude in line with the desorption energy that the contact parameter of MDPs should also be close to the here determined contact parameter. However, the contact parameter measured in the present study differs significantly from the value of 0.952 determined by Glandorf et al. [2002] for a water ice covered silicon surface which has been used in other studies of CO_2 nucleation in the Martian atmosphere [Colaprete et al., 2008; Listowski et al., 2014; Määttänen et al., 2007; Määttänen et al., 2005]. From the discussion in Glandorf et al. [2002] we estimate an uncertainty in their m value of approximately 2 %. The discrepancy to the value determined in this work could have several experimental reasons. The most obvious difference is that Glandorf et al. [2002] covered their surface with water-ice prior to introducing CO_2. The high contact parameter of 0.952 should then only be applicable to MDPs or MSPs which have acquired layers of water ice prior to the nucleation of CO_2. Water ice could nucleate prior to nucleation of CO_2 in the mesosphere of Mars. The lack of measurements of supersaturated conditions of water vapor above 50 km during the main occurrence season of CO_2 clouds however renders such a scenario unlikely [Maltagliati et al., 2011; Maltagliati et al., 2013], strengthening the relevance of our contact parameter for pure MSPs and MDPs in the mesosphere of Mars. Nevertheless, Vincendon et al. [2011] observed a water ice cloud at a height between 70 and 80 km, proving that under special conditions such a scenario could indeed be realistic. A second scenario for water ice covered particles would include MDPs acquiring a layer of water ice at altitudes below 50 km and getting advected to CO_2 cloud heights rapidly enough to avoid complete evaporation during subsaturated conditions. During the night, the combination of the dust maxima being located at heights between 15 – 30 km [Guzewich et al., 2013; Heavens et al., 2011a; Heavens et al., 2014; Heavens et al., 2011b; McCleese et al., 2010] and the CO_2 cloud height of 80 – 100 km cast this scenario into doubt, strengthening the possible importance of MSPs as nuclei. During day, CO_2 clouds occur at lower heights between 60 and 85 km and a second dust maximum at heights between 45 and 65 km [Guzewich et al., 2013] is present, allowing MDPs to be potential nuclei. In addition, Heavens et al [2015] observed extreme detached dust layers up to a height of 75 km near Olympus Mons and Tharsis Montes. However, the survival of water ice particles up to a height above 60 km would require very rapid convection.

Another possible explanation for the discrepancy with [Glandorf et al., 2002] is that they determined the contact parameter by observing CO_2 nucleation on a planar surface and not on nanometer-sized particles. The contact parameter m is a material property which, in theory, should be independent of the curvature of the substrate. It has to be noted that Glandorf et al. [2002] determined m at temperatures between 130 and 140 K, so a temperature dependence of m may be also a possible explanation. Indeed, a temperature-dependence of the contact parameter has been reported for water ice [Fortin et al., 2003; Iraci et al., 2010; Määttänen and Douspis, 2014; Phebus et al., 2011; Shilling et al., 2006; Trainer et al., 2009]. In order to explain the difference between our CO_2 ice measurements and Glandorf et al. [2002], a linear dependence of m on T should have a slope of approximately 0.0025 K^{-1} over the temperature span encompassing the ranges of both experiments (60 to 140 K). Within the 10 K range considered in each work, this would correspond to a change in m of the same order as the experimental uncertainty and could therefore have been obscured by noise. Thus, although a temperature dependence of m was observed neither by Glandorf et al. [2002] nor in our experiments, it cannot be excluded that the difference between the values of m determined in both experiments is caused by a temperature dependence.

4.2 Extrapolation to Martian mesospheric conditions

To put our results into context of the Martian atmosphere, we assume that the contact parameter as well as the desorption energy are independent of particle temperature. We use the parameters determined in this work and the nucleation theory described in Appendix A to extrapolate our results to Martian mesospheric conditions. Doing so, we calculated the nucleation activation temperature for a height profile in the Martian mesosphere. The term activation temperature is justified by a strong dependence of the nucleation rate on the particle temperature. Figure shows nucleation rates calculated using Equation (A1) and the measured mean desorption energy and contact parameter for different particle radii as a function of particle temperature. The calculations were performed at a constant CO_2 concentration of 10^{20} m^{-3} which corresponds to a height of approximately 70 km. A particle temperature change of 1 K modifies the nucleation rate by about 3 orders of magnitude for all particle sizes. Consequently, there is a very well defined temperature for each CO_2 concentration and particle size at which nucleation is induced. Since cold pockets in the Martian mesosphere have a lifetime in the order of hours [Listowski et al., 2014], we assume that a nucleation rate of $J = 0.01\ s^{-1}$ on abundant nuclei (50 % activated particles after 69 s) is sufficient to form clouds. The temperature at which $J = 0.01\ s^{-1}$ is in the following referred to as the nucleation activation temperature, which exhibits a strong size dependence for particles smaller than about 30 nm. As it can be seen in Figure , activating nucleation on 2 nm radius particles requires temperatures about 7 K colder compared to 30 nm particles.

We have used an exponential fit to the variation of density with height measured during the entry process of Pathfinder in 1997 [Magalhães et al., 1999] and assumed a CO_2 mixing ratio of 95 % in order to produce a CO_2 concentration profile of the Martian mesosphere. Then we have applied the nucleation parameterization presented above to calculate the height dependence of a representative activation temperature in the Martian mesosphere assuming a 2 nm radius particle representing MSPs. The result is shown as the green curve in Figure , where the shaded area represents the uncertainty range evaluated by varying the desorption energy as well as the contact parameter within their uncertainties. The saturation temperature is shown as a blue line according to which nucleation on a 2 nm particle is activated 14 to 18 K below the saturation temperature. We have also calculated the nucleation activation temperature as a function of height for a 30 nm particle, which is shown by the cyan colored curve in Figure . Here, nucleation is activated 8 to 10 K below saturation temperature. Since there is no strong dependence of activation temperature on particle sizes above 30 nm, the calculated nucleation activation temperature profile for a 30 nm particle can be seen as the upper nucleation activation temperature limit of pure MSPs as well as MDPs.

We have carried out the same calculations with a contact parameter of 0.952 representing water ice-covered particles [Glandorf et al., 2002]. In this case, nucleation would occur at about 5 to 7 K warmer temperatures as compared to particles without ice cover. One uncertainty in dealing with CO_2 ice clouds in the mesosphere of Mars is whether MSPs or MDPs act as nuclei. Night-time observations of temperatures as low as 20 K below saturation in the absence of clouds [Forget et al., 2009; Montmessin et al., 2011] can be explained by 3 scenarios: i) not enough nuclei are present, ii) a sufficient amount of potent nuclei is present but the particles cannot grow to sizes large enough to be observed due to a short exposure time to supersaturated conditions, and iii) a sufficient amount of nuclei is present, but the nucleation ability of the particles is too low to activate nucleation even in a highly supersaturated environment. The latter scenario indicates that during the night the nuclei are rather small (MSPs) and/or not covered with water ice. If the latter conclusion also holds for day-time, then the contact parameter and desorption energy describing the nucleation ability would be almost identical for both particle types and the importance of each particle type as nuclei would depend mainly on their particle size distribution in the mesosphere.

In summary, temperatures at least 8 K below the saturation temperature are needed in the Martian mesosphere to activate nucleation on nanoparticles which are not covered with water ice. Such cold temperatures are indeed observed. The Pathfinder entry temperature profile is shown by the black curve in Figure representing rather common temperatures below frost point at a height of about 80 km [Forget et al., 2009; Montmessin et al., 2011]. In this case nucleation would not occur. We additionally plotted in red the temperature profile of orbit 1205 (occ. #1205) obtained from [Montmessin et al., 2006], which represents an extraordinarily cold event. Here, according to our measurements, nucleation would be activated assuming that pre-existing particles larger than 2 nm in radius are present. This indeed could have been the case, since a detached layer at lower altitudes between 75 and 95 km (red shaded area) was observed, which was probably caused by nucleation in the cold pocket above. The cold temperatures required to activate nucleation can explain the night-time observations of temperatures well below saturation temperature in absence of clouds [Forget et al., 2009; Montmessin et al., 2011]. In the discussion above, we assumed a constant contact parameter, which is justified by our observations and the results reported by Glandorf et al. [2002]. However, a change of m with temperature could have been obscured by noise. A mean contact parameter of 0.85 would be valid at Martian mesospheric supersaturated conditions if we assume a linear change of m between the temperature range of Glandorf et al. [2002] and our measurements. Then, activation temperatures would be about 2 to 3 K warmer as compared to a contact parameter of 0.78.

4.3 Summary and Outlook

In this manuscript we presented pioneering measurements on heterogeneous nucleation on nanometer sized particles performed with the novel MICE-TRAPS apparatus. We determined the desorption energy to $\Delta F_{des} = (18.5 \pm 0.2)\ \mathrm{kJ\ mol^{-1}}$ and the contact parameter to 0.78 ± 0.02 for CO_2 nucleation on iron oxide and silica particles at temperatures close to the conditions encountered in the Martian mesosphere. In future, we will also be able to observe nucleation on magnesium oxide and mixed Mg-Fe-silicate particles in order to extend the set of parameters governing nucleation for a larger spectrum of possible MSP compositions [Saunders and Plane, 2011]. If the particle size distribution of MSPs and MDPs in the Martian mesosphere during day and night and the probability of their ice coverage in combination with typical temperature profiles are known, the major type of nuclei could be evaluated with the desorption energy and contact parameter presented here. Additionally, we suggest that these parameters are used in future model studies in order to compare the results with observations. MICE-TRAPS allows us to observe adsorption and nucleation on freely levitated particles in the size regime of several nanometers. To the best of the authors knowledge, measurements comparable to those presented here have never been performed before. Additionally, MICE-TRAPS allows the production of supersaturated conditions of other condensable gases such as H_2O vapor and hydrocarbons. Measurements on water vapor adsorption and nucleation are of great importance for water ice nucleation in the Martian atmosphere as well as for the formation of noctilucent clouds in the mesosphere of Earth and will be presented in forthcoming publications.

Appendix A: Nucleation Formalism and Growth Rate Theory

The nucleation and growth rate theory used throughout the literature differs in many details and aspects depending on the physical situation under investigation. In order to keep our results comprehensible we give a rather extensive account of the formulations used in our analysis of the nucleation and growth experiments in the following section. All parameters which are used in the data analysis and not explicitly described in the text are listed in Table A.1.

Appendix A.1: Nucleation Theory

We use classical heterogeneous nucleation induced by surface diffusion to describe the microphysical nucleation process in the Martian mesosphere. This approach assumes that the CO_2 molecules collide with the condensation nucleus and reside on it for a certain amount of time. Due to diffusion on the surface, CO_2 molecules can collide and combine to produce clusters of different sizes, which may eventually reach the critical size resulting in a nucleation event. We will discuss the most essential parts of this theory briefly here (a detailed description of the basic theoretical concepts can for example be found in [Pruppacher and Klett, 1997] or [Keesee, 1989]).

The heterogeneous nucleation rate induced by surface diffusion on the surface of a spherical nucleus is written as:

$$J_{het} = A_N f_{\delta T} Z_{het} \beta_{het} c_{1,s} \cdot exp\left(\frac{-\Delta F^*_{het}}{kT_N}\right)\ [s^{-1}] \tag{A1}$$

$A_N = 4\pi r_N^2$ is the surface area of the condensation nucleus, $f_{\delta T}$ the non-isothermal coefficient and $c_{1,s}$ the concentration of monomers on the particle surface. The diffusional flux of molecules on the particle surface to the critical cluster is described by β_{het}, and the heterogeneous Zeldovic factor Z_{het} accounts for the dissociation of super-critical clusters. T_N is the temperature of the condensation nucleus, k the Boltzmann constant and ΔF^*_{het} the free energy of forming a critical cluster on the surface of the condensation nucleus, described by:

$$\Delta F^*_{het} = f(m,x) \cdot \Delta F^*_{hom} = f(m,x) \cdot \frac{4\pi\sigma r_{crit}^2}{3} \tag{A2}$$

The homogeneous free energy of formation ΔF^*_{hom} of a spherical cluster with radius r_{crit} is deduced from the Gibbs-Thomson equation. The reduction of the free energy of formation for heterogeneous nucleation is described by $f(m,x)$, where $m = \cos\theta$ is the contact parameter which is a measure of the nucleation ability of the particle material and is related to the contact angle between the condensation nucleus and the nucleating phase, and x is the ratio of the size of the condensation nucleus and the corresponding critical cluster size.

The concentration of monomers $c_{1,s}$ on the surface of the nucleus is calculated from the incoming and outgoing flux of CO_2 molecules by assuming a steady state

$$c_{1,s} = \frac{p_{CO_2}}{\upsilon\sqrt{2\pi m_{CO_2} kT_N}} \cdot exp\left(\frac{\Delta F_{des}}{kT_N}\right) \tag{A3}$$

where υ is the vibrational frequency of a CO_2 molecule on the surface of the condensation nucleus. The desorption energy ΔF_{des} is a characteristic property of the condensation nucleus material. A change in ΔF_{des} of only 20 % results in a variation of the nucleation rate by about 5 orders of magnitude at typical conditions in the Martian mesosphere. This demonstrates the need for ΔF_{des} to be determined for each nucleus material.

The non-isothermal coefficient $f_{\delta T}$ accounts for the released heat of sublimation during embryo growth, which offsets the embryo temperature with respect to the ambient temperature. As a result, the nucleation rate is reduced by a factor $f_{\delta T} < 1$. In the experiments described below, a binary gas mixture of He/CO_2 is present at a pressure ratio of 100:1 and higher. This ensures isothermal conditions as validated in [Duft et al., 2015], and $f_{\delta T}$ may be assumed to be unity for the analysis of the experimental results. The efficiency of heat dissipation from the embryo is greatly reduced when the nucleating species is also the main atmospheric component. This is the case in the atmosphere of Mars, where CO_2 constitutes about 95% of the gaseous compounds. Anyway, for heterogeneous nucleation, the close contact of embryo and nucleus increases the efficiency of heat dissipation such that $f_{\delta T}$ can be assumed to be 1 for condensation nuclei larger as the critical cluster [Määttänen et al., 2007].

Appendix A.2: Growth Rate Theory

Through dynamic processes such as sedimentation and temporal temperature variations, the time for nanoparticles to grow to detectable sizes in supersaturated conditions in the Martian

mesosphere is limited. The sticking probability or sticking coefficient α is an important parameter governing the rate of depositional mass accretion on nanoparticles. The sticking coefficient is defined as the probability that a molecule is adsorbed when hitting a surface and is the equivalent of Maxwell's mass accommodation coefficient. Data on the sticking coefficient of CO_2 as function of the temperature is rare, but can be evaluated by analyzing the depositional CO_2 growth rate on nanoparticles as we will show below.
Our experiment operates in the free molecular regime, i.e. the mean free path of molecules in the gas phase is larger than the spatial distance between the source of the CO_2 molecules (the ice-covered surfaces) and the particles. The depositional growth of vapor phase molecules on the particle surface is thus not limited by diffusion of molecules through a viscous medium. As shown in [Duft et al., 2015] and detailed above, the background pressure of helium gas is still high enough to ensure isothermal conditions during CO_2 nucleation and growth. Therefore, a simple growth model is used which compares the flux of incoming to the flux of outgoing CO_2 molecules:

$$\frac{dm}{dt} = [\alpha \cdot j_{in} - j_{out}(t)] \cdot A_c(t) \cdot m_{CO_2} \tag{A4}$$

Here, m_{CO_2} is the mass of a CO_2 molecule, $A_c(t) = 4\pi\left(r_p + r_{CO_2}\right)^2$ is the effective surface area describing the collision of a CO_2 molecule with the particle and r_p is the time dependent particle radius. The hard sphere collision radius of a CO_2 molecule r_{CO_2} may not be neglected here due to the small size of the particles investigated ($r_p = 2$ nm). The incoming flux density $j_{in} = n_{CO_2} \cdot v_{th}/4$ is given by the concentration n_{CO_2} and the mean thermal velocity v_{th} of CO_2 molecules. The flux density emitted from the curved particle surface j_{out} is given by the Kelvin Equation. It can be expressed using the sticking coefficient and the saturation vapor pressure p_{sat} at particle temperature T_{part} resulting in

$$\frac{dm}{dt} = \frac{v_{th} \cdot p_{sat}}{4\,k\,T_{part}} \cdot \alpha \cdot \left[S - S_{eq}(t)\right] \cdot A_c(t) \cdot m_{CO_2} \tag{A5}$$

Here, $S = p_{CO_2}/p_{sat}$ denotes the nominal saturation at particle temperature and $S_{eq}(t)$ is the equilibrium saturation over the curved particle surface. In growth regime, the equilibrium saturation is a function of the changing particle size and therefore not constant in time. Assuming spherical particle growth, the only unknown quantity is the sticking coefficient. It must be pointed out that the growth rate parameterization shown above cannot be applied to the Martian mesosphere, where near-pure vapor condensation at high supersaturation takes place [Listowski et al., 2013].

Appendix A.3: Influence of Particle Charge

Charged particles as used in the presented experiments further interact with adsorbed molecules than neutral particles due to the interaction of the particle charge with the permanent or induced molecular dipole moment. This can lead to an increase in nucleation and growth rates gaining importance for smaller particles. CO_2 molecules do not have a permanent dipole moment, but can be polarized in the electric field of the charged particle with a mean polarizability of a CO_2 molecule of $2.6\,\text{Å}^3$ [Alms et al., 1975]. Consequently, charge-dipole interaction can be neglected and only charge-induced dipole interaction has to be considered. However, the energy of the induced dipole in the electric field on the surface of a singly charged r=2 nm particle is about $2 \cdot 10^{-4}$ eV per molecule which compares to desorption and sublimation energy of 0.2 eV and 0.26 eV, respectively. We therefore conclude that charge-induced dipole interaction can be neglected for nucleation and growth of CO_2 vapor in our experiments.

Acknowledgments and Data

All data used to generate the results of this paper is available upon request from the corresponding author.

The authors thank the German Federal Ministry of Education and Research (BMBF, grant number 05K13VH3), the German Research Foundation (DFG, grant number LE 834/4-1) and the European Research Council (project number 291332) for financial support of this work. TPM thanks the United Kingdom Natural Environment Research Council for providing studentship funding. This research received support from the QualityNano Project which is financed by European Community Research Infrastructure Action under the FP7 "Capacities" Program.

We would like to thank Anni Määttänen for very valuable comments which helped to improve the manuscript.

References

Adolfsson, L. G., B. A. S. Gustafson, and C. D. Murray (1996), The Martian atmosphere as a meteoroid detector, Icarus, 119(1), 144-152.

Alms, G. R., A. K. Burnham, and W. H. Flygare (1975), Measurement of Dispersion in Polarizability Anisotropies, Journal of Chemical Physics, 63(8), 3321-3326.

Azreg-Ainou, M. (2005), Low-temperature data for carbon dioxide, Mon. Chem., 136(12), 2017-2027.

Bardeen, C. G., O. B. Toon, E. J. Jensen, D. R. Marsh, and V. L. Harvey (2008), Numerical simulations of the three-dimensional distribution of meteoric dust in the mesosphere and upper stratosphere, J. Geophys. Res.-Atmos., 113(D17).

Baumann, W., B.-S. Thedekar, H.-R. Paur, and H. Seifert (2006), Characterization of Nanoparticles Synthesized in the Microwave Plasma Discharge Process by Particle Mass Spectrometry and Transmission Electron Microscopy, in AIChE Annual Meeting, edited, San Francisco.

Clancy, R. T., and B. J. Sandor (1998), CO2 ice clouds in the upper atmosphere of Mars, Geophys. Res. Lett., 25(4), 489-492.

Clancy, R. T., M. J. Wolff, B. A. Whitney, B. A. Cantor, and M. D. Smith (2007), Mars equatorial mesospheric clouds: Global occurrence and physical properties from Mars Global Surveyor Thermal Emission Spectrometer and Mars Orbiter Camera limb observations, J. Geophys. Res.-Planets, 112(E4).

Colaprete, A., J. R. Barnes, R. M. Haberle, and F. Montmessin (2008), CO2 clouds, CAPE and convection on Mars: Observations and general circulation modeling, Planet Space Sci., 56(2), 150-180.

Creasey, J. E., J. M. Forbes, and D. P. Hinson (2006), Global and seasonal distribution of gravity wave activity in Mars' lower atmosphere derived from MGS radio occultation data, Geophys. Res. Lett., 33(1).

Duft, D., M. Nachbar, M. Eritt, and T. Leisner (2015), A Linear Trap for Studying the Interaction of Nanoparticles with Supersaturated Vapors, Aerosol Sci. Technol., 49(9), 683-691.

Fletcher, N. H. (1958), Size Effect in Heterogeneous Nucleation, Journal of Chemical Physics, 29(3), 572-576.

Forget, F., and R. T. Pierrehumbert (1997), Warming early Mars with carbon dioxide clouds that scatter infrared radiation, Science, 278(5341), 1273-1276.

Forget, F., R. Wordsworth, E. Millour, J. B. Madeleine, L. Kerber, J. Leconte, E. Marcq, and R. M. Haberle (2013), 3D modelling of the early martian climate under a denser CO2 atmosphere: Temperatures and CO2 ice clouds, Icarus, 222(1), 81-99.

Forget, F., F. Montmessin, J. L. Bertaux, F. Gonzalez-Galindo, S. Lebonnois, E. Quemerais, A. Reberac, E. Dimarellis, and M. A. Lopez-Valverde (2009), Density and temperatures of the upper Martian atmosphere measured by stellar occultations with Mars Express SPICAM, J. Geophys. Res.-Planets, 114.

Fortin, T. J., K. Drdla, L. T. Iraci, and M. A. Tolbert (2003), Ice condensation on sulfuric acid tetrahydrate: Implications for polar stratospheric ice clouds, Atmospheric Chemistry and Physics, 3, 987-997.

Giesen, B., H. Wiggers, A. Kowalik, and P. Roth (2005), Formation of Si-nanoparticles in a microwave reactor: Comparison between experiments and modelling, J. Nanopart. Res., 7(1), 29-41.

Glandorf, D. L., A. Colaprete, M. A. Tolbert, and O. B. Toon (2002), CO2 snow on Mars and early Earth: Experimental constraints, Icarus, 160(1), 66-72.

Gonzalez-Galindo, F., A. Määttänen, F. Forget, and A. Spiga (2011), The martian mesosphere as revealed by CO2 cloud observations and General Circulation Modeling, Icarus, 216(1), 10-22.

Guzewich, S. D., E. R. Talaat, A. D. Toigo, D. W. Waugh, and T. H. McConnochie (2013), High-altitude dust layers on Mars: Observations with the Thermal Emission Spectrometer, J. Geophys. Res.-Planets, 118(6), 1177-1194.

Heavens, N. G., D. J. McCleese, M. I. Richardson, D. M. Kass, A. Kleinbohl, and J. T. Schofield (2011a), Structure and dynamics of the Martian lower and middle atmosphere as observed by the Mars Climate Sounder: 2. Implications of the thermal structure and aerosol distributions for the mean meridional circulation, J. Geophys. Res.-Planets, 116.

Heavens, N. G., M. S. Johnson, W. A. Abdou, D. M. Kass, A. Kleinbohl, D. J. McCleese, J. H. Shirley, and R. J. Wilson (2014), Seasonal and diurnal variability of detached dust layers in the tropical Martian atmosphere, J. Geophys. Res.-Planets, 119(8), 1748-1774.

Heavens, N. G., B. A. Cantor, P. O. Hayne, D. M. Kass, A. Kleinbohl, D. J. McCleese, S. Piqueux, J. T. Schofield, and J. H. Shirley (2015), Extreme detached dust layers near Martian volcanoes: Evidence for dust transport by mesoscale circulations forced by high topography, Geophys. Res. Lett., 42(10), 3730-3738.

Heavens, N. G., M. I. Richardson, A. Kleinbohl, D. M. Kass, D. J. McCleese, W. Abdou, J. L. Benson, J. T. Schofield, J. H. Shirley, and P. M. Wolkenberg (2011b), The vertical distribution of dust in the Martian atmosphere during northern spring and summer: Observations by the Mars Climate Sounder and analysis of zonal average vertical dust profiles, J. Geophys. Res.-Planets, 116.

Herr, K. C., and G. C. Pimentel (1970), Evidence for solid carbon dioxide in upper atmosphere of Mars, Science, 167(3914), 47-&.

Hirschfelder, J., C. F. Curtiss, and R. B. Bird (1966), Molecular Theory of Gases and Liquids, 1280 pp., John Wiley & Sons.

Iraci, L. T., B. D. Phebus, B. M. Stone, and A. Colaprete (2010), Water ice cloud formation on Mars is more difficult than presumed: Laboratory studies of ice nucleation on surrogate materials, Icarus, 210(2), 985-991.

James, P. B., H. H. Kieffer, and D. A. Paige (1992), The seasonal cycle of carbon dioxide on Mars, in Mars, edited by H. H. Kieffer, pp. 934-368, University of Arizona Press.

Janzen, C., H. Kleinwechter, J. Knipping, H. Wiggers, and P. Roth (2002), Size analysis in low-pressure nanoparticle reactors: comparison of particle mass spectrometry with in situ probing transmission electron microscopy, J. Aerosol. Sci., 33(6), 833-841.

Keesee, R. G. (1989), Nucleation and Particle Formation in the Upper-Atmosphere, J. Geophys. Res.-Atmos., 94(D12), 14683-14692.

Listowski, C., A. Maattanen, I. Riipinen, F. Montmessin, and F. Lefevre (2013), Near-pure vapor condensation in the Martian atmosphere: CO2 ice crystal growth, J Geophys Res-Planet, 118(10), 2153-2171.

Listowski, C., A. Määttänen, F. Montmessin, A. Spiga, and F. Lefèvre (2014), Modeling the microphysics of CO2 ice clouds within wave-induced cold pockets in the martian mesosphere, Icarus, 237, 239-261.

Luna, R., C. Millan, C. Santonja, and M. A. Satorre (2009), Triple test under high vacuum conditions to control the reliability of thin ice film accretion and desorption for astrophysical applications, Vacuum, 83(6), 942-948.

Määttänen, A., and M. Douspis (2014), Estimating the variability of contact parameter temperature dependence with the Monte Carlo Markov Chain method, GeoResJ, 3–4, 46-55.

Määttänen, A., H. Vehkamaki, A. Lauri, I. Napari, and M. Kulmala (2007), Two-component heterogeneous nucleation kinetics and an application to Mars, J. Chem. Phys., 127(13).

Määttänen, A., H. Vehkamäki, A. Lauri, S. Merikallio, J. Kauhanen, H. Savijärvi, and M. Kulmala (2005), Nucleation studies in the Martian atmosphere, J. Geophys. Res.-Planets, 110(E2).

Määttänen, A., et al. (2010), Mapping the mesospheric CO2 clouds on Mars: MEx/OMEGA and MEx/HRSC observations and challenges for atmospheric models, Icarus, 209(2), 452-469.

Magalhães, J. A., J. T. Schofield, and A. Seiff (1999), Results of the Mars Pathfinder atmospheric structure investigation, J. Geophys. Res.-Planets, 104(E4), 8943-8955.

Maltagliati, L., F. Montmessin, A. Fedorova, O. Korablev, F. Forget, and J. L. Bertaux (2011), Evidence of Water Vapor in Excess of Saturation in the Atmosphere of Mars, Science, 333(6051), 1868-1871.

Maltagliati, L., F. Montmessin, O. Korablev, A. Fedorova, F. Forget, A. Määttänen, F. Lefèvre, and J. L. Bertaux (2013), Annual survey of water vapor vertical distribution and water-aerosol coupling in the martian atmosphere observed by SPICAM/MEx solar occultations, Icarus, 223(2), 942-962.

McCleese, D. J., et al. (2010), Structure and dynamics of the Martian lower and middle atmosphere as observed by the Mars Climate Sounder: Seasonal variations in zonal mean temperature, dust, and water ice aerosols, J. Geophys. Res.-Planets, 115.

Meinen, J., S. Khasminskaya, E. Rühl, W. Baumann, and T. Leisner (2010), The TRAPS Apparatus: Enhancing Target Density of Nanoparticle Beams in Vacuum for X-ray and Optical Spectroscopy, Aerosol Sci. Technol., 44(4), 316-328.

Mischna, M. A., J. F. Kasting, A. Pavlov, and R. Freedman (2000), Influence of carbon dioxide clouds on early martian climate, Icarus, 145(2), 546-554.

Montmessin, F., F. Forget, F. Bertaux, J.-L. Spiga, and A. Määttänen (2011), Existence of Supercold Atmospheric Layers in the Martian Mesosphere, 404-405.

Montmessin, F., B. Gondet, J. P. Bibring, Y. Langevin, P. Drossart, F. Forget, and T. Fouchet (2007), Hyperspectral imaging of convective CO2 ice clouds in the equatorial mesosphere of Mars, J. Geophys. Res.-Planets, 112(E11).

Montmessin, F., et al. (2006), Subvisible CO2 ice clouds detected in the mesosphere of Mars, Icarus, 183(2), 403-410.

Morris, R. V., et al. (2000), Mineralogy, composition, and alteration of Mars Pathfinder rocks and soils: Evidence from multispectral, elemental, and magnetic data on terrestrial analogue, SNC meteorite, and Pathfinder samples, J. Geophys. Res.-Planets, 105(E1), 1757-1817.

Phebus, B. D., A. V. Johnson, B. Mar, B. M. Stone, A. Colaprete, and L. T. Iraci (2011), Water ice nucleation characteristics of JSC Mars-1 regolith simulant under simulated Martian atmospheric conditions, J Geophys Res-Planet, 116.

Plane, J. M. C., W. Feng, and E. C. M. Dawkins (2015), The Mesosphere and Metals: Chemistry and Changes, Chemical Reviews, 115(10), 4497-4541.

Pruppacher, H. R., and J. D. Klett (1997), Microphysics of Clouds and Precipitation, Kluwer Academic Publishers, Dordrecht.

Sandford, S. A., and L. J. Allamandola (1990), The physical and infrared spectral properties of CO2 in astrophysical ice analogs, Astrophys. J., 355(1), 357-372.

Saunders, R. W., and J. M. C. Plane (2011), A photo-chemical method for the production of olivine nanoparticles as cosmic dust analogues, Icarus, 212(1), 373-382.

Seki, J., and H. Hasegawa (1983), The heterogeneous condensation of interstellar ice grains, Astrophys. Space Sci., 94(1), 177-189.

Shilling, J. E., T. J. Fortin, and M. A. Tolbert (2006), Depositional ice nucleation on crystalline organic and inorganic solids, J. Geophys. Res.-Atmos., 111(D12).

Smith, P. H., et al. (1997), Results from the Mars Pathfinder camera, Science, 278(5344), 1758-1765.

Souda, R. (2006), Glass-liquid transition of carbon dioxide and its effect on water segregation, J. Phys. Chem. B, 110(36), 17884-17888.

Spiga, A., F. Gonzalez-Galindo, M. A. Lopez-Valverde, and F. Forget (2012), Gravity waves, cold pockets and CO2 clouds in the Martian mesosphere, Geophys. Res. Lett., 39.

Trainer, M. G., O. B. Toon, and M. A. Tolbert (2009), Measurements of Depositional Ice Nucleation on Insoluble Substrates at Low Temperatures: Implications for Earth and Mars, J. Phys. Chem. C, 113(6), 2036-2040.

Vehkamäki, H., A. Määttänen, A. Lauri, I. Napari, and M. Kulmala (2007), Technical Note: The heterogeneous Zeldovich factor, Atmos. Chem. Phys., 7(2), 309-313.

Vincendon, M., C. Pilorget, B. Gondet, S. Murchie, and J. P. Bibring (2011), New near-IR observations of mesospheric CO2 and H2O clouds on Mars, J. Geophys. Res.-Planets, 116.

Vondrak, T., J. M. C. Plane, S. Broadley, and D. Janches (2008), A chemical model of meteoric ablation, Atmospheric Chemistry and Physics, 8(23), 7015-7031.

Weida, M. J., J. M. Sperhac, and D. J. Nesbitt (1996), Sublimation dynamics of CO2 thin films: A high resolution diode laser study of quantum state resolved sticking coefficients, Journal of Chemical Physics, 105(2), 749-766.

Whalley, C. L., and J. M. C. Plane (2010), Meteoric ion layers in the Martian atmosphere, Faraday Discuss., 147, 349-368.

Wood, S. E. (1999), Nucleation and Growth of CO2 Ice Crystals in the Martian Atmosphere, Phd thesis, University of California, Los Angeles.

Wordsworth, R., F. Forget, E. Millour, J. W. Head, J. B. Madeleine, and B. Charnay (2013), Global modelling of the early martian climate under a denser CO2 atmosphere: Water cycle and ice evolution, Icarus, 222(1), 1-19.

Zent, A. P., and R. C. Quinn (1995), Simultaneous adsorption of CO2 and H2O under Mars-like conditions and application to the evolution of the Martian climate, J. Geophys. Res.-Planets, 100(E3), 5341-5349.

Table 1: List of measurements carried out for the determination of the desorption energy (r_{part} = particle radius, T_{part} = particle temperature, n_{CO2} = CO_2 number density, S = saturation at particle location, m_{ads} = measured adsorbed mass of CO_2 molecules, and $c_{1,s\ norm}$ = normalized surface concentration).

Experiment	Run	r_{part} [Morris et al.]	T_{part} [K]	n_{CO_2} $[10^{15}\ m^{-3}]$	S	m_{ads} $[10^{-23}\ kg]$	$c_{1,s\ norm}$ $[10^3\ m]$
Silica particles							
133	86-90	2.82 ± 0.05	69.44 ± 0.35	10.2 ± 1.1	567 ± 142	9.02 ± 0.27	1.21 ± 0.14
133	71-73	2.44 ± 0.04	67.2 ± 0.35	3.98 ± 0.40	961 ± 251	7.43 ± 0.27	3.42 ± 0.34
133	68-70	2.77 ± 0.05	67.18 ± 0.35	3.92 ± 0.39	985 ± 258	8.72 ± 0.25	3.17 ± 0.32
134	92-95	3.05 ± 0.05	68.82 ± 0.38	6.14 ± 0.58	510 ± 136	10.7 ± 0.1	2.05 ± 0.20
134	96-99	3.32 ± 0.06	69.09 ± 0.38	6.13 ± 0.59	428 ± 113	11.9 ± 0.2	1.92 ± 0.19
134	128-131	3.55 ± 0.06	69.55 ± 0.35	6.14 ± 0.59	318 ± 78	13.1 ± 0.3	1.85 ± 0.18
134	110-112	3.55 ± 0.06	69.55 ± 0.35	6.25 ± 060	323 ± 79	13.6 ± 0.5	1.88 ± 0.20
136	123-125	2.42 ± 0.04	67.66 ± 0.35	4.86 ± 0.48	881 ± 227	8.93 ± 0.17	3.42 ± 0.34
136	126-127	2.52 ± 0.04	67.65 ± 0.35	4.94 ± 0.48	900 ± 232	9.82 ± 0.14	3.40 ± 0.33
136	130-131	2.70 ± 0.05	67.95 ± 0.34	4.85 ± 0.48	718 ± 179	11.1 ± 0.4	3.43 ± 0.36
140	82-84	2.51 ± 0.04	66.25 ± 0.35	2.65 ± 0.29	1274 ± 346	9.71 ± 0.12	6.33 ± 0.70
140	110-112	2.50 ± 0.04	69.41 ± 0.36	10.2 ± 1.1	578 ± 148	7.57 ± 0.17	1.29 ± 0.14
140	132-135	2.48 ± 0.04	71.99 ± 0.37	35.7 ± 3.4	405 ± 98	6.99 ± 0.21	0.35 ± 0.03
140	113-115	2.76 ± 0.05	69.44 ± 0.35	10.2 ± 1.1	567 ± 142	8.55 ± 0.72	1.20 ± 0.16
Iron oxide particles							
112	134	1.89 ± 0.03	68.65 ± 0.36	10.0 ± 1.1	935 ± 245	4.53 ± 0.12	1.38 ± 0.16
112	208	1.95 ± 0.03	68.70 ± 0.36	9.79 ± 1.1	881 ± 232	4.01 ± 0.14	1.17 ± 0.14
112	162	2.00 ± 0.03	68.78 ± 0.36	9.96 ± 1.1	850 ± 222	4.27 ± 0.13	1.16 ± 0.13
112	198	2.09 ± 0.04	68.70 ± 0.36	9.83 ± 1.1	883 ± 226	4.10 ± 0.17	1.04 ± 0.12
112	176	2.15 ± 0.04	68.83 ± 0.36	9.73 ± 1.1	802 ± 210	4.36 ± 0.16	1.06 ± 0.13
113	74	2.20 ± 0.04	68.67 ± 0.37	10.5 ± 1.1	859 ± 255	5.41 ± 0.21	1.17 ± 0.13
113	164	2.29 ± 0.04	68.81 ± 0.36	10.4 ± 1.0	873 ± 223	5.49 ± 0.18	1.10 ± 0.11
114	66	1.87 ± 0.03	68.22 ± 0.40	10.2 ± 1.0	1269 ± 361	4.76 ± 0.18	1.45 ± 0.15
117	189	1.97 ± 0.03	69.58 ± 0.41	19.2 ± 1.8	977 ± 274	5.08 ± 0.19	0.74 ± 0.08
117	197	1.99 ± 0.03	69.41 ± 0.41	19.2 ± 1.8	1086 ± 305	5.18 ± 0.49	0.74 ± 0.10
117	205	2.04 ± 0.03	69.83 ± 0.41	19.3 ± 1.8	831 ± 231	6.16 ± 0.29	0.83 ± 0.09
117	214	2.11 ± 0.04	69.75 ± 0.41	19.1 ± 1.8	869 ± 242	6.78 ± 0.27	0.87 ± 0.09
130	112	1.97 ± 0.03	66.90 ± 0.36	3.94 ± 0.39	1203 ± 324	7.14 ± 0.21	5.10 ± 0.53
130	116	2.09 ± 0.04	66.90 ± 0.36	3.90 ± 0.38	1188 ± 319	7.29 ± 0.15	4.65 ± 0.46

Table 2: List of measurements used for sticking coefficient analysis (r_{part} = particle radius, T_{part} = particle temperature, n_{CO2} = CO_2 number density, S = saturation at particle location, α = sticking coefficient).

Experiment	Run	r_{part} [Morris et al.]	T_{part} [K]	n_{CO_2} $[10^{15}\ m^{-3}]$	S	α
Silica particles						
133	59-61	2.78 ± 0.05	64.55 ± 0.39	4.01 ± 0.40	6690 ± 2060	0.62 ± 0.06
133	107-111	2.78 ± 0.05	68.64 ± 0.41	4.10 ± 0.37	3840 ± 1100	0.48 ± 0.04
133	56-58	2.47 ± 0.04	64.53 ± 0.39	3.98 ± 0.39	6720 ± 2070	0.69 ± 0.07
133	102-106	2.47 ± 0.04	68.63 ± 0.41	4.12 ± 0.36	3890 ± 1110	0.53 ± 0.05
134	65-68	3.00 ± 0.05	63.28 ± 0.44	6.36 ± 0.57	27800 ± 9900	1.04 ± 0.10
136	147-149	2.75 ± 0.05	67.14 ± 0.39	14.6 ± 1.3	3750 ± 1070	0.78 ± 0.08
136	141-143	2.44 ± 0.04	67.11 ± 0.39	15.0 ± 4.3	3950 ± 1550	0.80 ± 0.08
136	144-146	2.53 ± 0.04	67.11 ± 0.39	14.6 ± 1.3	38660 ± 1100	0.81 ± 0.08
136	80-83	2.44 ± 0.04	64.05 ± 0.41	4.75 ± 0.45	11540 ± 3760	0.92 ± 0.09
140	58-60	2.51 ± 0.04	62.02 ± 0.42	2.52 ± 0.25	30100 ± 10700	0.86 ± 0.09
140	90-92	2.50 ± 0.04	66.20 ± 0.39	9.96 ± 0.98	4980 ± 1470	0.75 ± 0.08
140	93-95	2.78 ± 0.05	66.25 ± 0.39	9.90 ± 0.97	4760 ± 1400	0.79 ± 0.08
140	119-122	2.54 ± 0.04	68.42 ± 0.41	34.8 ± 3.2	3780 ± 1090	0.69 ± 0.07
Iron oxide particles						
115	62-67	1.89 ± 0.03	64.27 ± 0.41	4.06 ± 0.39	8360 ± 2710	1.02 ± 0.10
117	122-129	2.10 ± 0.04	67.11 ± 0.44	19.0 ± 1.7	5000 ± 1590	0.99 ± 0.09
117	98-105	2.12 ± 0.04	67.11 ± 0.44	19.3 ± 1.7	5080 ± 1610	0.80 ± 0.07
117	114-121	1.89 ± 0.03	67.08 ± 0.44	19.1 ± 1.7	5160 ± 1640	0.90 ± 0.09
117	138-145	2.05 ± 0.03	67.08 ± 0.44	19.1 ± 1.7	5160 ± 1640	0.91 ± 0.09
130	77-84	1.97 ± 0.03	63.07 ± 0.32	3.79 ± 0.35	19610 ± 5240	1.02 ± 0.10

Table 3: List of measurements carried out for the determination of the nucleation rate and the contact parameter (r_{part} = particle radius, T_{part} = particle temperature, n_{CO2} = CO_2 number density, S = saturation at particle location, m_{ads} = measured critical adsorbed mass of CO_2 molecules, J = estimated nucleation rate and m = contact parameter).

Experiment	Run	r_{part} [Morris et al.]	T_{part} [K]	n_{CO_2} $[10^{15}\ m^{-3}]$	S	m_{ads} $[10^{-22}\ kg]$	J $[s^{-1}]$	m
Silica particles								
133	74-77	2.45 ± 0.04	67.85 ± 0.37	12.0 ± 1.1	1914 ± 510	1.05	0.20	0.777 ± 0.026
134	79-82	3.04 ± 0.05	68.03 ± 0.38	6.18 ± 0.58	873 ± 238	1.44	0.14	0.790 ± 0.026
136	104-105	2.44 ± 0.04	66.42 ± 0.37	4.94 ± 0.48	2104 ± 587	1.26	0.17	0.783 ± 0.026
136	132-134	2.53 ± 0.04	68.73 ± 0.37	14.7 ± 1.4	1295 ± 339	1.27	0.33	0.788 ± 0.026
136	138-140	2.75 ± 0.05	68.70 ± 0.37	14.6 ± 1.4	1295 ± 339	1.34	0.40	0.778 ± 0.025
140	75-76	2.52 ± 0.04	65.09 ± 0.37	2.58 ± 0.24	2869 ± 841	1.23	0.08	0.772 ± 0.026
140	102-105	2.53 ± 0.04	67.60 ± 0.37	9.97 ± 1.00	1882 ± 511	1.14	0.29	0.778 ± 0.025
140	127-130	2.54 ± 0.04	69.57 ± 0.87	34.4 ± 3.2	1756 ± 459	1.09	0.67	0.769 ± 0.025
Iron oxide particles								
114	76-85	1.89 ± 0.03	66.54 ± 0.41	9.92 ± 0.95	3885 ± 1181	0.83	0.5	0.793 ± 0.027
115	47-55	1.93 ± 0.03	66.57 ± 0.41	10.06 ± 0.94	3857 ± 1169	0.70	0.5	0.791 ± 0.027
115	62-67	1.89 ± 0.03	64.26 ± 0.41	4.06 ± 0.39	8361 ± 2710	0.69	0.17	0.772 ± 0.027
117	223-230	1.99 ± 0.03	70.29 ± 0.45	70.0 ± 5.9	2259 ± 668	0.50	0.5	0.787 ± 0.027
117	231-238	2.13 ± 0.04	70.46 ± 0.44	69.8 ± 5.9	2030 ± 586	0.38	0.67	0.785 ± 0.026
117	239-247	1.99 ± 0.03	73.04 ± 0.48	346.3 ± 26	2113 ± 612	0.59	0.67	0.768 ± 0.027
117	248-253	2.13 ± 0.04	73.00 ± 0.48	346.7 ± 26	2172 ± 630	0.24	0.67	0.764 ± 0.027

Table A.1: Summary of parameters not described explicitly in Section 3

Parameter	Symbol	Unit	Value	Reference
Equations				
Thermal velocity	v_{th}	$m\ s^{-1}$	$\sqrt{\frac{8kT_{part}}{\pi m_{CO_2}}}$	-
Saturation vapor pressure	p_{sat}	Pa	$1.38 \cdot 10^{12}\ exp\left(\frac{-3182.48}{T_{part}}\right)$	[Azreg-Ainou, 2005; James et al., 1992]
Equilibrium saturation over the curved particle surface	S_{eq}	-	$exp\left(\frac{2m_{CO_2}\sigma}{kT_{part}\rho_{CO_2}r_{part}}\right)$	[Pruppacher and Klett, 1997]
CO_2 vapor pressure	p_{CO_2}	Pa	$n_{CO_2}kT_{part}$	-
Number of molecules in a critical cluster	n^*_{crit}	-	$4\pi r^3_{crit}\rho_{CO_2}/(3m_{CO_2})$	-
Critical germ radius	r_{crit}	m	$\frac{2m_{CO_2}\sigma}{\rho_{CO_2}kT_N ln(S)}$	[Pruppacher and Klett, 1997]
Surface diffusion growth coefficient	β_{het}	s^{-1}	$2\pi r_{crit}\sin\theta\ dc_{1,s} \cdot \upsilon \cdot exp\left(\frac{-\Delta F_{sd}}{kT_N}\right)$	[Pruppacher and Klett, 1997]
Reduction of the free energy of formation for heterogeneous nucleation	$f(m,x)$	-	$0.5 \cdot \begin{bmatrix} 1+\left(\frac{1-mx}{\Phi}\right)^3 \\ +x^3(2-3k+k^3) \\ +3mx^2(k-1) \end{bmatrix}$ $k = \frac{x-m}{\Phi}$ $\Phi = \sqrt{1-2mx+x^2}$ $x = \frac{r_N}{r_{crit}}$	[Fletcher, 1958]
Heterogeneous Zeldovich factor	Z_{het}	-	$Z_{hom} \cdot \sqrt{\frac{4}{2+\frac{(1-mx)[2-4mx-(m^2-3)x^2]}{(1-2mx+x^2)^{3/2}}}}$	[Vehkamäki et al., 2007]
Homogeneous Zeldovich factor	Z_{hom}	-	$\sqrt{\frac{\Delta F^*_{hom}}{3\pi kT_N {n^*_{crit}}^2}}$	[Pruppacher and Klett, 1997]
Constants				
Surface tension of dry ice	σ	$N\ m^{-1}$	0.08	[Wood, 1999]
Density of dry ice at (T=55-80) K	ρ_{CO_2}	$g\ cm^{-3}$	1.5	[Luna et al., 2009]
CO_2 vibrational frequency	υ	s^{-1}	$2.9 \cdot 10^{12}$	[Sandford and Allamandola, 1990]
Energy of surface diffusion	ΔF_{sd}	$J\ molec^{-1}$	$\frac{\Delta F_{des}}{10}$	[Seki and Hasegawa, 1983]
Mean jumping distance of a CO_2 molecule	d	nm	0.4	[Wood, 1999]
Hard sphere collision radius of CO_2	r_{CO_2}	nm	0.197	[Hirschfelder et al., 1966]

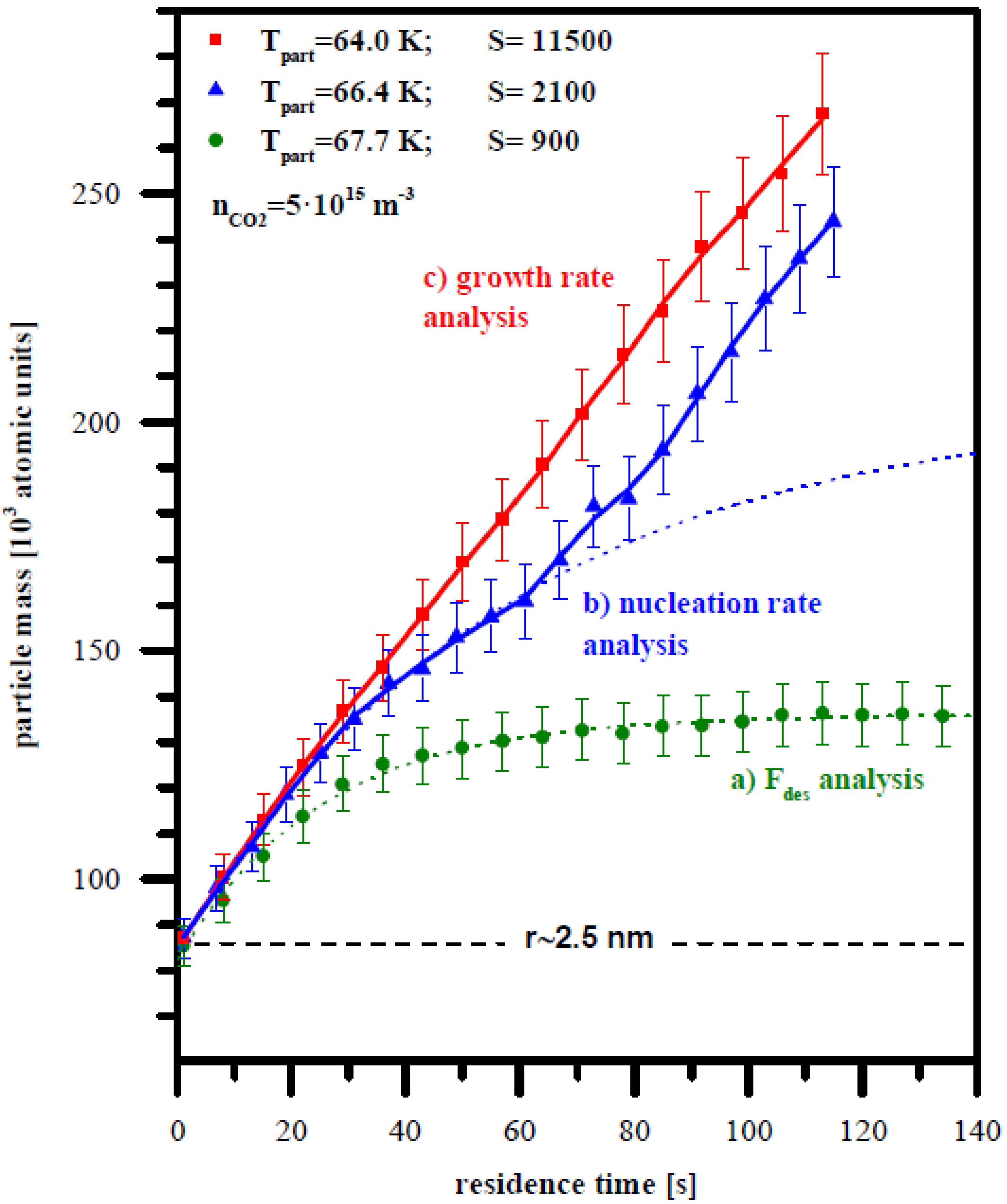

Figure 1: Series of CO_2 deposition measurements on 2.5 nm radius silica particles at constant CO_2 concentration. By decreasing temperature, and thus increasing saturation, the deposition regime can be changed from adsorption only (curve a) to delayed nucleation and subsequent growth (curve b) and to immediate growth (curve c).

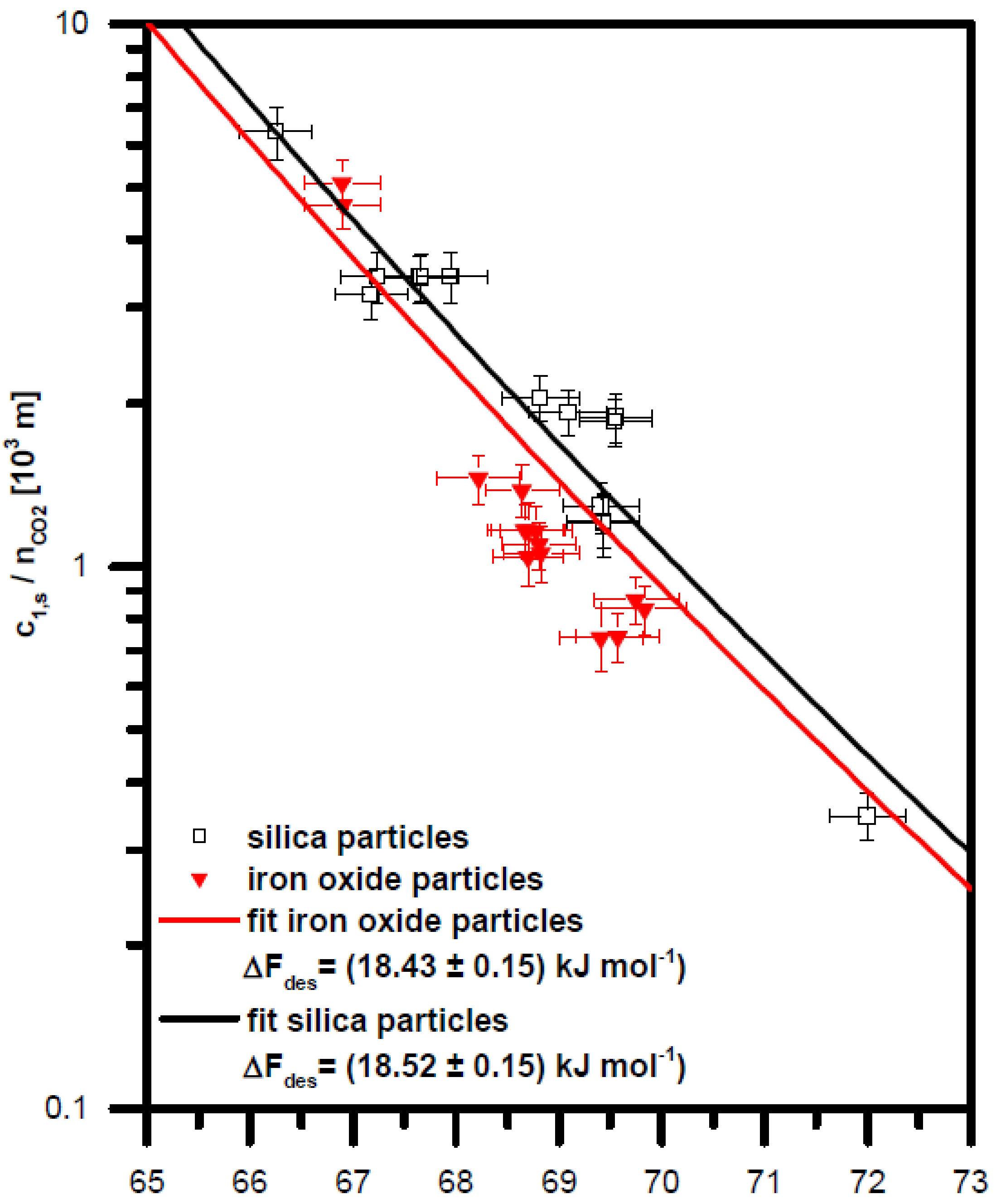

Figure 2: Surface concentration of adsorbed CO_2 molecules normalized to the ambient CO_2 concentration as a function of particle temperature. Measurements were performed on iron oxide (triangles) and on silica particles (squares). The lines represent separate fits of the desorption energy to the measurements on iron oxide particles (red) and silica particles (black), respectively.

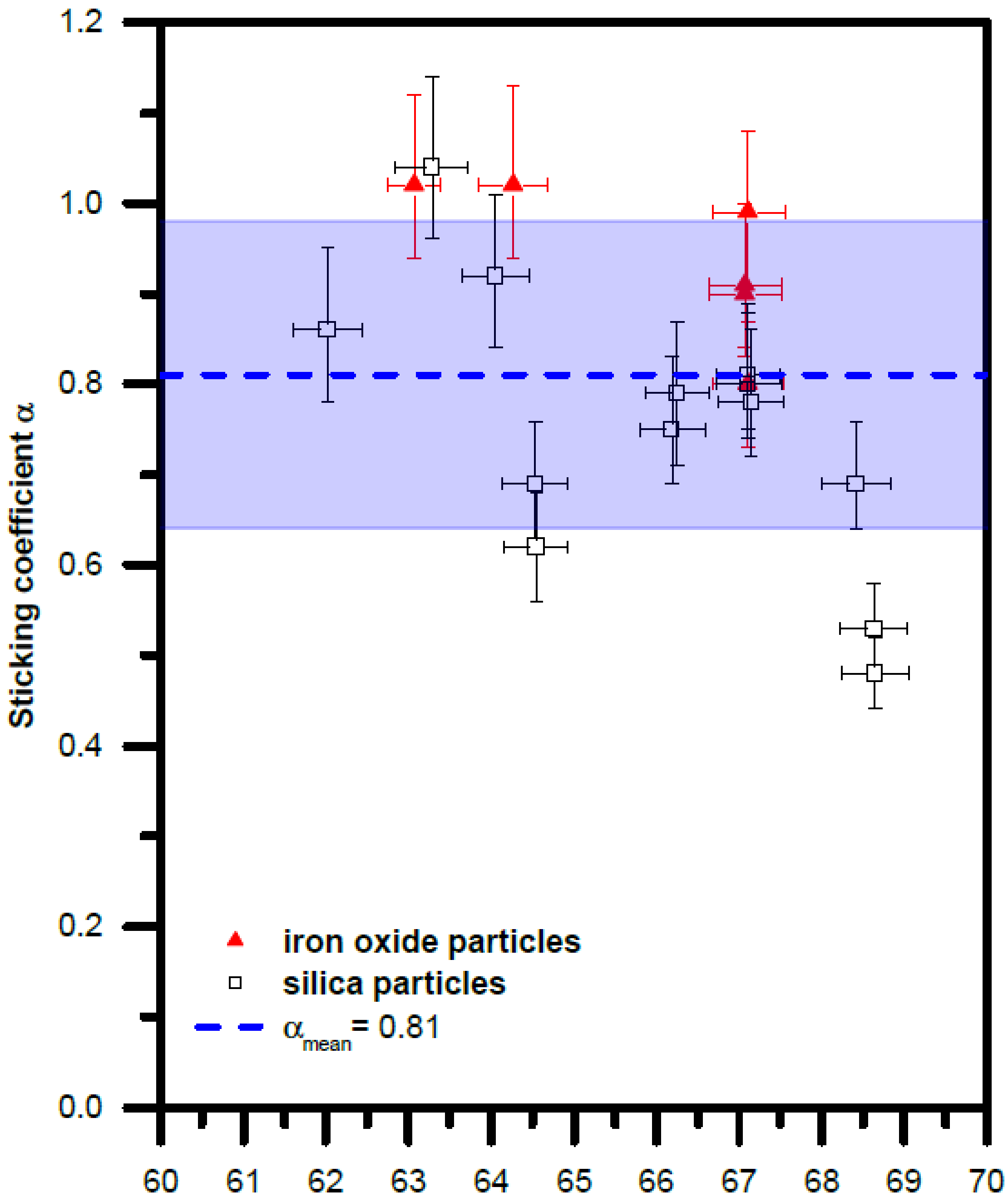

Figure 3: Sticking coefficient of CO_2 as a function of particle temperature. Shown are measurements on iron oxide (triangles) and on silica particles (squares). The blue dashed line and shaded area represent the determined mean value of 0.81±0.17.

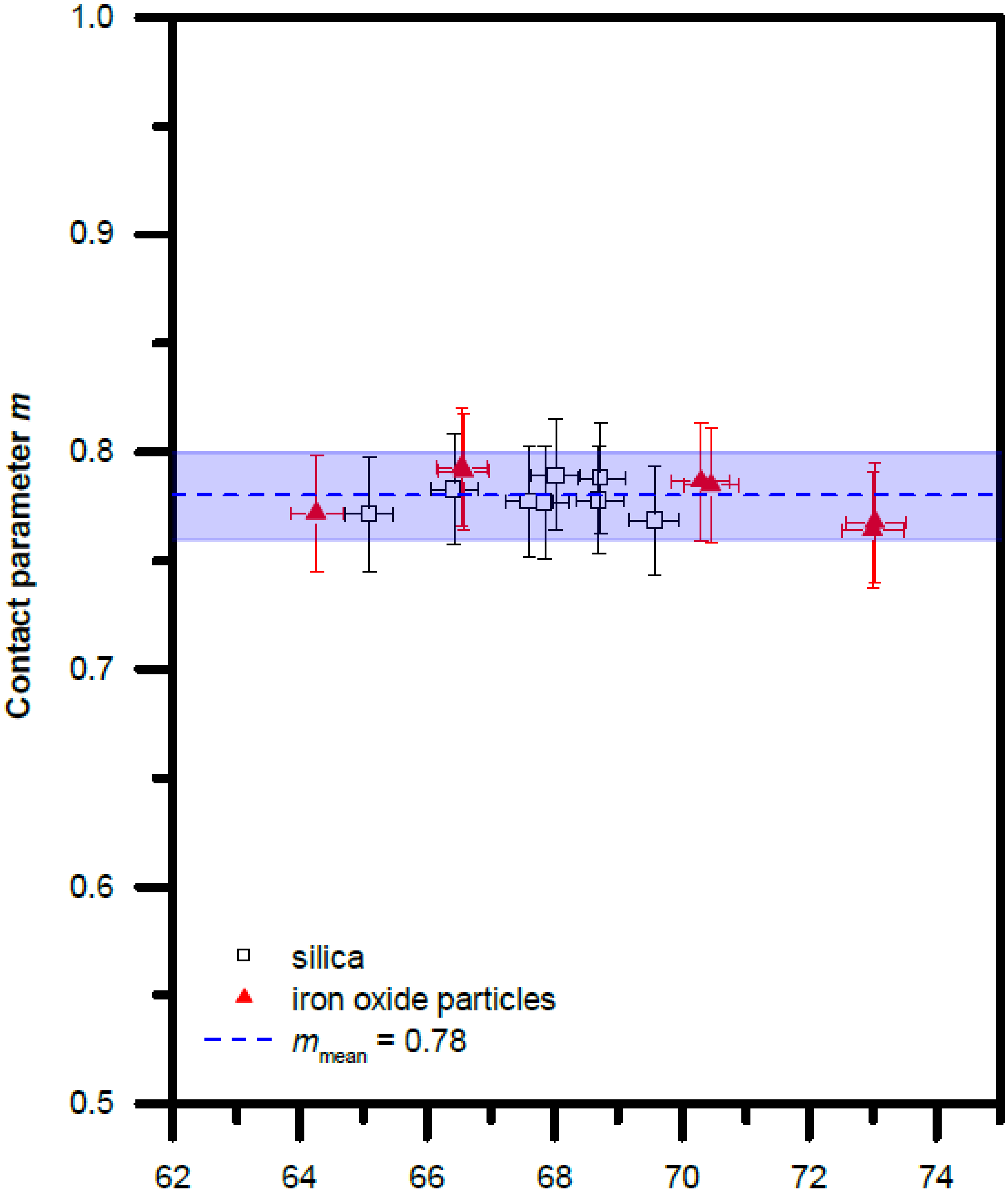

Figure 4: Contact parameter as a function of particle temperature for iron oxide particles (triangles) and silica particles (squares). The blue dashed line and shaded area represent the determined mean value of 0.78±0.02.

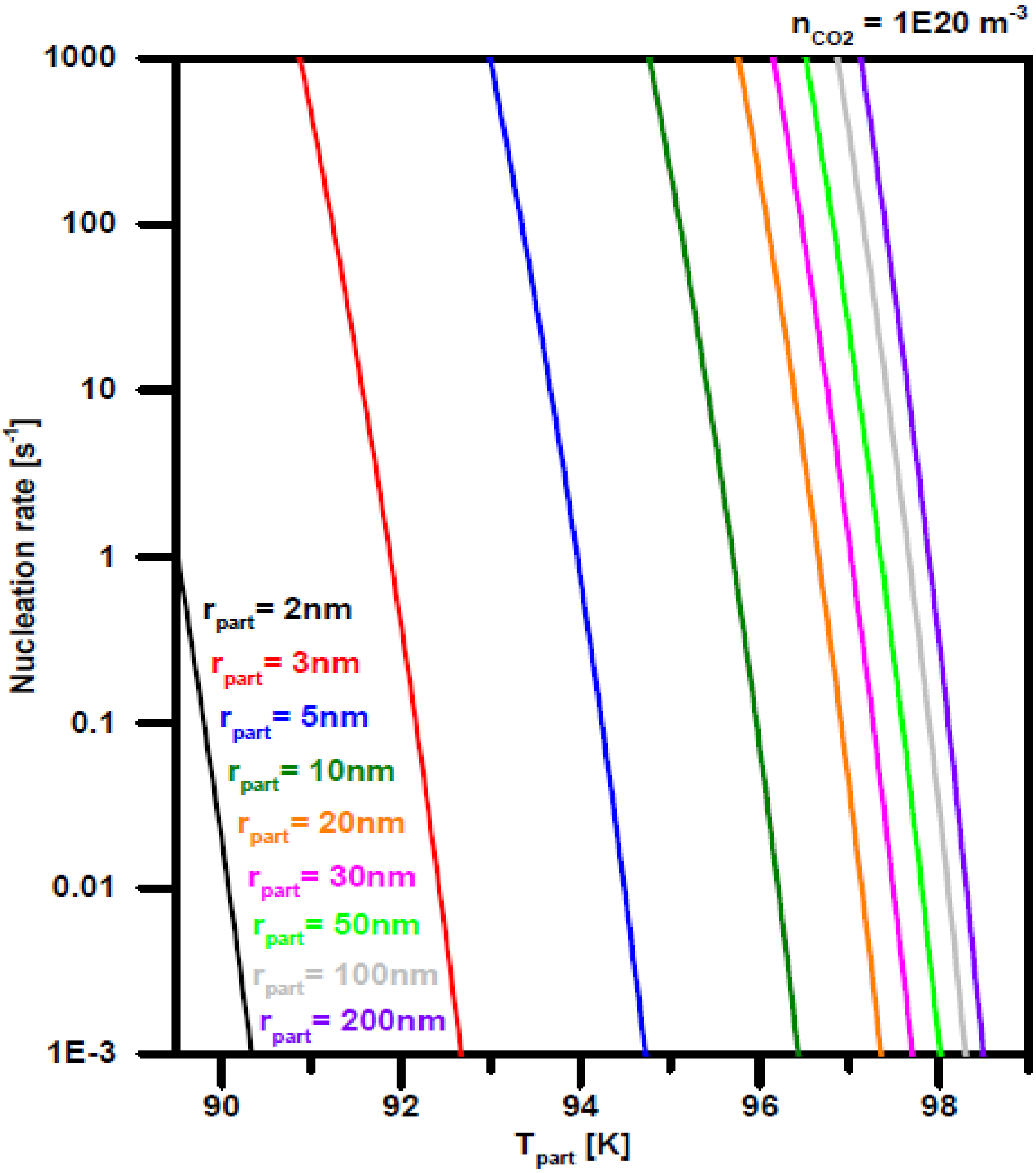

Figure 5: Calculated nucleation rates at typical Martian mesospheric conditions ($\boldsymbol{n_{CO_2}} = \mathbf{10^{20}\ m^{-3}}$) as a function of particle temperature for several particle sizes. The experimentally determined mean values of $\Delta \boldsymbol{F_{des}}$ and m are used.

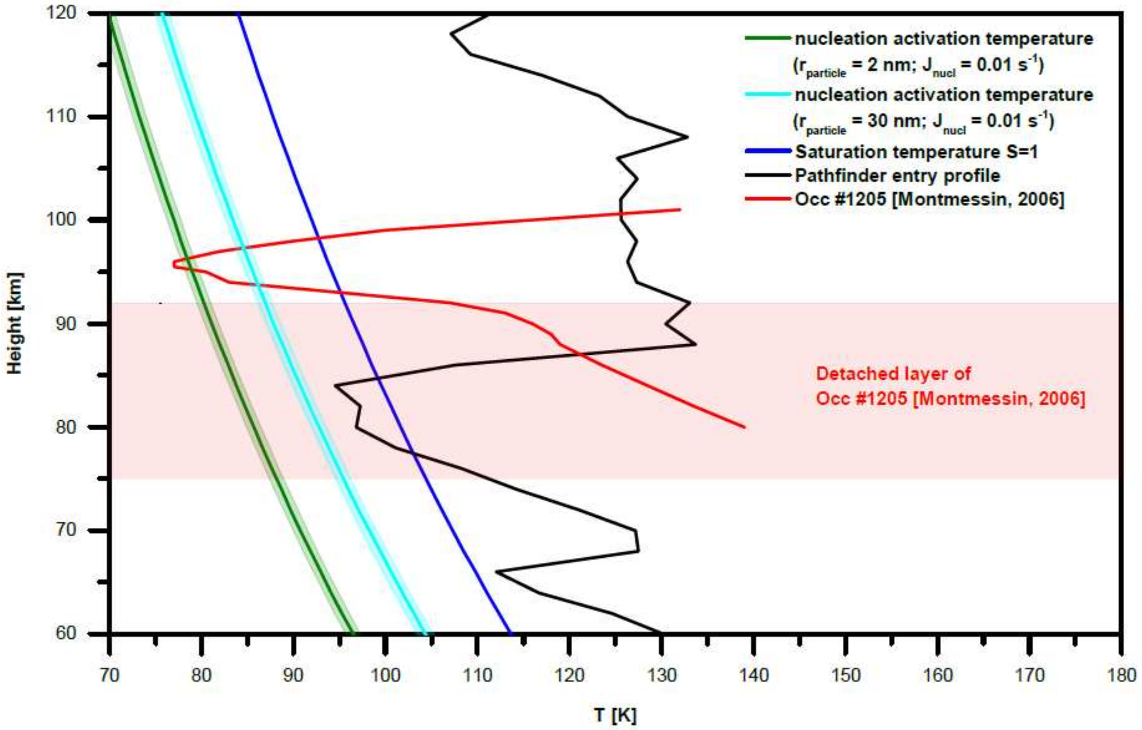

Figure 6: Calculated nucleation activation temperature with height for a 2 nm (green curve) and 30 nm particle (cyan curve). For comparison, the Saturation temperature (blue curve) as well as two measured temperature profiles, the Pathfinder entry profile [Magalhães et al., 1999] and orbit 1205 (occ. #1205) of [Montmessin et al., 2006], are shown. Additionally, the area of the detached layer observed during the measurement of occ. #1205 is indicated with the red shaded area.